

## TWO-FLUID NUMERICAL SIMULATIONS OF SOLAR SPICULES

BŁAŻEJ KUŹMA,<sup>1</sup> KRIS MURAWSKI,<sup>1</sup> PRADEEP KAYSHAP,<sup>1</sup> DAREK WÓJCIK,<sup>1</sup> ABHISHEK KUMAR SRIVASTAVA,<sup>2</sup> AND BHOLA N. DWIVEDI<sup>2</sup>

<sup>1</sup>*Group of Astrophysics, University of Maria Curie-Skłodowska, ul. Radziszewskiego 10, 20-031 Lublin, Poland*

<sup>2</sup>*Department of Physics, Indian Institute of Technology (BHU), Varanasi-221005, India*

Submitted to ApJ

### ABSTRACT

We aim to study the formation and evolution of solar spicules by means of numerical simulations of the solar atmosphere. With the use of newly developed JOANNA code, we numerically solve two-fluid (for ions + electrons and neutrals) equations in 2D Cartesian geometry. We follow the evolution of a spicule triggered by the time-dependent signal in ion and neutral components of gas pressure launched in the upper chromosphere. We use the potential magnetic field, which evolves self-consistently, but mainly plays a passive role in the dynamics. Our numerical results reveal that the signal is steepened into a shock that propagates upward into the corona. The chromospheric cold and dense plasma lags behind this shock and rises into the corona with a mean speed of 20-25 km s<sup>-1</sup>. The formed spicule exhibits the upflow/downfall of plasma during its total lifetime of around 3-4 minutes, and it follows the typical characteristics of a classical spicule, which is modeled by magnetohydrodynamics. The simulated spicule consists of a dense and cold core that is dominated by neutrals. The general dynamics of ion and neutral spicules are very similar to each other. Minor differences in those dynamics result in different widths of both spicules with increasing rarefaction of the ion spicule in time.

*Keywords:* Sun: activity — Sun: corona — Sun: transition region — magnetohydrodynamics (MHD) — methods: numerical

arXiv:1711.01383v1 [astro-ph.SR] 4 Nov 2017

## 1. INTRODUCTION

Spicules are thin jet-like structures, which dominate in the lower layers of the solar corona. They are best seen at the solar limb in strong chromospheric and transition-region (TR) spectral lines such as  $H\alpha$ ,  $Ca\ II\ H\ \&\ K$ ,  $Mg\ II\ H\ \&\ K$ ,  $C\ II$  and  $Si\ IV$  lines (e.g., Roberts 1945; Matsuno & Hirayama 1988; Nishikawa 1988; Suematsu et al. 1995; De Pontieu et al. 2007b; Suematsu et al. 2008; Sterling et al. 2010; Madjarska et al. 2011; Pereira et al. 2012; Tsiropoula et al. 2012; Skogsrud et al. 2014, 2015; Pereira et al. 2014; Ruppe van der Voort et al. 2015; Pereira et al. 2016; Beck et al. 2016). Spicule observations have been carried out for about 130 years since they were first reported in 1877 (Secchi 1887). Therefore, a huge amount of observational literature about spicules is available, which is dedicated to understanding their basic properties (mass density, temperature, velocity, and magnetic field), initiation mechanisms, waves, and oscillations. These crucial aspects are very well documented in various review papers, i.e., basic properties by Beckers (1968, 1972) and Suematsu (1998), initiation mechanisms by Sterling (2000), and oscillations and waves by Zaqarashvili & Erdélyi (2009).

High-resolution observational data leads to continuous improvement of our knowledge about the spicules. Based on their properties, De Pontieu et al. (2007b) classified the spicules into two different categories (i.e., Types I and II). Type I spicules exhibit a slower velocity ( $15\text{-}40\text{ km s}^{-1}$ ) and longer lifetime (3-10 minutes) compared to the velocity ( $30\text{-}110\text{ km s}^{-1}$ ) and lifetime (50-150 s) of Type II spicules. Type I spicules reveal the rise and fall of plasma during its total life, while type II spicules fade from the view and the downfall of plasma is not visible (e.g., De Pontieu et al. 2007b; Pereira et al. 2012). Sterling & Hollweg (1984) have proposed that the heating rate is sufficient to heat the spicules to temperatures at which the hydrogen is fully ionized. Therefore,  $H\text{-}\alpha$  spicules (cool temperature) may evolve into EUV spicules (hot temperature). Later, this thermal evolution (i.e., fading of the spicules from cool filters and appears in the hot filters) of the spicules was investigated in various other works as well (e.g., De Pontieu et al. 2009; McIntosh & De Pontieu 2009; McIntosh et al. 2010; Tian et al. 2011). Recently, Pereira et al. (2014) have reported the traces of spicules in the hot temperature filter after fading from the cool temperature filter.

The origin and excitation mechanisms of spicules are one of the most crucial issues of solar physics, which has been continuously investigated using observations as well as numerical simulations. Pulses in velocity or gas pressure, Alfvén waves, and p-modes are the three broad categories of drivers that may be responsible for the formation of spicules. Main physical process within the velocity/gas pressure pulse model is the formation of a shock front, which results in a generation of the spicule in the

lower corona. Such a rebound shock model was developed by Hollweg (1982) who used a gas pressure pulse in one-dimensional (1D) MHD equations for the formation of a spicule. In another approach, Suematsu et al. (1982) performed a numerical experiment using a velocity pulse instead of a gas pressure pulse. Later, this rebound shock model was improved by including radiation and heat conduction in the model (e.g., Sterling & Mariska 1990; Cheng 1992; Sterling et al. 1993; Heggland et al. 2007; Kužma et al. 2017). Recently, Sterling & Moore (2016) have reported that the microfilament-eruptions can be a potential candidate for the generation of spicules. Murawski & Zaqarashvili (2010) performed 2D numerical simulations with a velocity pulse to produce the spicule. Multistructural, bidirectional flows and 3-5 minute periodicity in the occurrence of spicules were successfully reproduced in that numerical experiment. This model was extended into its 2D counterpart with the inclusion of the nonadiabatic effects (Kužma et al. 2017). A general conclusion drawn from the performed simulations was that the shocks play an important role in the dynamics and thermodynamics of impulsively generated spicules and the other nonadiabatic terms (i.e., thermal conduction and radiative cooling terms) produce minor effects on the dynamics/thermodynamics of the spicule.

In the second category, it was proposed that the nonlinear coupling between Alfvén waves and slow magnetoacoustic shocks can lift up the TR, which produces the spicule (Hollweg et al. 1982). This idea for the generation of spicules was further investigated by Cranmer & Woolsey (2015, 2016). They have found that the magnetohydrodynamic turbulence is a potential driver for spicules. It was also reported that the random nonlinear Alfvén pulses may reproduce the spicules (Kudoh & Shibata 1999). More interestingly, the damping of Alfvén waves due to ion-neutral collisions can be an efficient mechanism for the formation of spicules in the solar atmosphere (Haerendel 1992; James et al. 2003).

In the third category, De Pontieu et al. (2004) showed that p-modes are the potential candidates for triggering spicules in the solar atmosphere, which was further investigated in various other works (e.g., Hansteen et al. 2006; De Pontieu et al. 2007a).

The above mentioned main three categories (i.e., gas pressure or velocity pulse, Alfvén waves and p-modes) are not the only mechanisms for the formation of spicules. Indeed, there are various other numerous proposed physical processes responsible for the formation of spicules. Among others, the compression of the plasma sheet by the magnetic field (Hollweg 1972), Joule heating in the current sheet (Hirayama 1992), thermal conduction from the corona (Kopp & Kuperus 1968; Moore & Fung 1972) and buffeting of anchored magnetic flux by granulation can lead to spicules

(Roberts 1979). These and various other mechanisms are discussed by Sterling (2000).

Although spicules were discovered a long time ago (Secchi 1887), they are still not fully understood. Therefore, they remain subject of further investigation. Advanced numerical simulations are an important means to reveal the nature of spicules. However, it is always difficult to implement the real solar conditions in the numerical experiment. Because low layers of the solar atmosphere contain large fraction of neutrals (e.g., Zaqarashvili et al. 2011), two-fluid plasma (i.e., ionized and neutral fluids) approach in the numerical experiment is more suitable than magnetohydrodynamics (MHD) to study the evolution of spicules in the solar atmosphere. This approach is used for the first time in the present numerical simulations of solar spicules. Specifically, we perform 2D numerical simulations of two-fluid equations to produce the spicule using pulses launched initially in vertical components of ion and neutral velocities. The adopted potential magnetic field configuration plays essentially a passive role in the present simulations. The paper is organized as follows. In Section 2, we describe the physical model of the solar atmosphere. Numerical simulations are presented in Section 3. Summary and conclusions are outlined in the last section.

## 2. PHYSICAL MODEL OF THE SOLAR ATMOSPHERE

### 2.1. Two-fluid Equations

We consider a gravitationally stratified and magnetically confined plasma that consists of two components: ionized fluid (ions + electrons) and neutral fluid (neutrals). This model is governed by the following set of equations (Smith & Sakai 2008):

$$\frac{\partial \varrho_i}{\partial t} + \nabla \cdot (\varrho_i \mathbf{V}_i) = -\varrho_i(\alpha_r \varrho_i - \alpha_i \varrho_n), \quad (1)$$

$$\frac{\partial \varrho_n}{\partial t} + \nabla \cdot (\varrho_n \mathbf{V}_n) = \varrho_i(\alpha_r \varrho_i - \alpha_i \varrho_n), \quad (2)$$

$$\varrho_i \left( \frac{\partial \mathbf{V}_i}{\partial t} + (\mathbf{V}_i \cdot \nabla) \mathbf{V}_i \right) = -\nabla p_i + \frac{1}{\mu} (\nabla \times \mathbf{B}) \times \mathbf{B} + \varrho_i \mathbf{g} - \alpha_c \varrho_i \varrho_n (\mathbf{V}_i - \mathbf{V}_n) - \varrho_i (\alpha_r \varrho_i \mathbf{V}_i - \alpha_i \varrho_n \mathbf{V}_n), \quad (3)$$

$$\varrho_n \left( \frac{\partial \mathbf{V}_n}{\partial t} + (\mathbf{V}_n \cdot \nabla) \mathbf{V}_n \right) = -\nabla p_n + \varrho_n \mathbf{g} + \alpha_c \varrho_i \varrho_n (\mathbf{V}_i - \mathbf{V}_n) + \varrho_i (\alpha_r \varrho_i \mathbf{V}_i - \alpha_i \varrho_n \mathbf{V}_n), \quad (4)$$

$$\frac{\partial p_i}{\partial t} + \mathbf{V}_i \cdot \nabla p_i + \gamma p_i \nabla \cdot \mathbf{V}_i = (\gamma - 1) \alpha_c \varrho_i \varrho_n (\mathbf{V}_i - \mathbf{V}_n) \cdot \mathbf{V}_i, \quad (5)$$

$$\frac{\partial p_n}{\partial t} + \mathbf{V}_n \cdot \nabla p_n + \gamma p_n \nabla \cdot \mathbf{V}_n = (\gamma - 1) \alpha_c \varrho_i \varrho_n (\mathbf{V}_i - \mathbf{V}_n) \cdot \mathbf{V}_n, \quad (6)$$

$$\frac{\partial \mathbf{B}}{\partial t} = \nabla \times (\mathbf{V} \times \mathbf{B}), \quad \nabla \cdot \mathbf{B} = 0, \quad (7)$$

where  $\varrho_{i,n}$  is the mass density,  $p_{i,n}$  the gas pressure,  $\mathbf{V}_{i,n}$  represents the plasma velocity,  $\mathbf{B}$  is the magnetic field,  $\alpha_i$  is a coefficient of ionization,  $\alpha_r$  coefficient of recombination, and  $\alpha_c$  coefficient of collisions between particles, subscripts  $i$  and  $n$  correspond, respectively, to ions and neutrals,  $\gamma = 5/3$  is the adiabatic index, and  $\mathbf{g} = (0, -g, 0)$  is the gravitational acceleration. The value of  $g$  is equal to  $274 \text{ m s}^{-2}$ . For the sake of simplicity, all electron-components are neglected due to the small mass of electrons in relation to ions and neutrals.

### 2.2. Equilibrium Solar Atmosphere

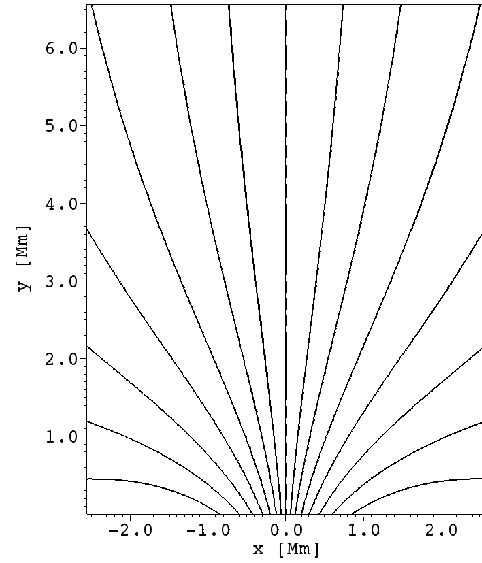


Figure 1. Magnetic field lines at the plasma equilibrium.

In a static solar atmosphere, all plasma quantities are time-invariant, which means that  $\partial f / \partial t = 0$ , where  $f$  denotes an equilibrium plasma quantity. Then, from Equations (1)-(7), it follows that for still ions ( $\mathbf{V}_i = \mathbf{0}$ ) and neutrals ( $\mathbf{V}_n = \mathbf{0}$ ) the Lorentz force (if appropriate) must be balanced by the gravity force and the gas pressure gradient,

$$\frac{1}{\mu} (\nabla \times \mathbf{B}) \times \mathbf{B} - \nabla p_{i,n} + \varrho_{i,n} \mathbf{g} = \mathbf{0}. \quad (8)$$

#### 2.2.1. Current-Free Magnetic Field and the Hydrostatic Atmosphere

A hydrostatic atmosphere for ions corresponds to the force-free ( $(\nabla \times \mathbf{B}) \times \mathbf{B} = \mathbf{0}$ ) magnetic field with the solenoidal condition ( $\nabla \cdot \mathbf{B} = 0$ ) being satisfied. We additionally assume a current-free ( $\nabla \times \mathbf{B} = \mathbf{0}$ ) magnetic field whose horizontal

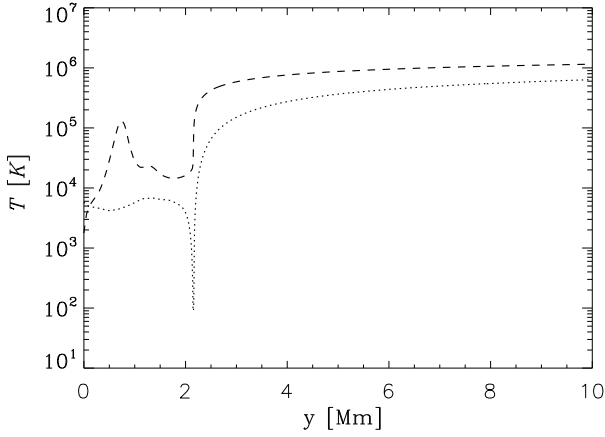


**Figure 2.** Vertical profiles of hydrostatic temperature of ions (dashed line) and neutrals (dotted line) vs. height  $y$ .

$B_x$ , vertical  $B_y$ , and transversal  $B_z$  components are given as (Konkol et al. 2012)

$$\begin{aligned} B_x(x, y) &= \frac{-2Sx(y-a)}{(x^2 + (y-a)^2)^2}, \\ B_y(x, y) &= \frac{S(x^2 - (y-a)^2)}{(x^2 + (y-a)^2)^2} + B_v, \\ B_z(x, y) &= 0, \end{aligned} \quad (9)$$

where  $B_v$  is a straight vertical magnetic field component,  $a$  and  $S$  are free parameters corresponding to the vertical location of the singularity in the magnetic field and the magnetic field strength, respectively. We set  $B_v = 6$  Gs,  $a = -1.5$  Mm and  $S$  in such a way that at the reference point ( $x_r = 0$ ,  $y_r = 10$ ) Mm the magnitude of magnetic field  $B = 8$  Gs. The corresponding magnetic field lines are displayed in Figure 1. We note that the magnetic field lines become less divergent with height.

For a force-free magnetic field it follows from Eq. (8) that at the equilibrium the gas pressure gradients have to be balanced by the gravity force,

$$\nabla p_{i,n} = \varrho_{i,n} \mathbf{g}. \quad (10)$$

With the use of the ideal gas law and the vertical,  $y$ -component of Eq. (10), we express the hydrostatic gas pressures and mass densities of ions and neutrals as

$$\begin{aligned} p_{i,n}(y) &= p_{0,i,n} \exp\left(-\int_{y_r}^y \frac{dy'}{\Lambda_{i,n}(y')}\right), \\ \varrho_{i,n}(y) &= \frac{p_{i,n}(y)}{g\Lambda_{i,n}(y)}, \end{aligned} \quad (11)$$

where

$$\Lambda_{i,n}(y) = \frac{k_B T_{i,n}(y)}{mg} \quad (12)$$

are the pressure scale heights of ions ( $\Lambda_i$ ) and neutrals ( $\Lambda_n$ ), and  $p_{0,i,n}$  denotes the gas pressure of ions and neutrals at the reference level,  $y = y_r = 10$  Mm. In Equation (12),  $T_i(y)$  and  $T_n(y)$  stand for temperatures of ions and neutrals, respectively. These temperatures are taken from the model of Avrett & Loeser (2008) (see Figure 2). Note that for  $y > 0.2$  Mm the temperature of ions is higher than the temperature of the neutrals. In the photosphere, which is localized at  $0 \leq y \leq 0.5$  Mm,  $T_i(y)$  increases with  $y$  until close to the bottom of the chromosphere, specifically for  $y \approx 0.7$  Mm,  $T_i(y)$  reaches its local maximum of about  $1.5 \cdot 10^5$  K. Higher up  $T_i(y)$  decreases with height until at the TR it rises abruptly to the coronal value of about 1 MK. The neutral temperature attains its value of about 5 kK within the region of  $0 \leq y \leq 1.75$  Mm. It decreases suddenly right below the TR attaining its minimum of about 150 K and higher up it increases with  $y$  reaching its coronal magnitude of about 0.8 MK at  $y = 10$  Mm.

As a result of the adopted temperature profiles, the mass densities of ions and neutrals decline with height. The left panel of Figure 3 shows the ratio of the mass density of ions to the mass density of neutrals,  $\varrho_i(x, y)/\varrho_n(x, y)$ , which result from Eq. (11). Note that below the level of  $y = 2.1$  Mm the plasma is dominated by neutrals with a minimum of  $\varrho_i/\varrho_n \approx 10^{-4}$ , while the corona consists of essentially fully ionized plasma; we added a small amount of neutrals in the solar corona due to numerical reasons. We specify the plasma  $\beta$  as the ratio of ion plus neutral gas pressures to magnetic pressure,

$$\beta(y) = \frac{p_i(y) + p_n(y)}{B^2(y)/2\mu}. \quad (13)$$

The spatial profile of plasma  $\beta$  is illustrated in the right panel of Figure 3. Note that within the displayed region for the coronal plasma, for  $y > 2.1$  Mm, and along the entire  $x = 0$  line  $\beta$  is smaller than 1.

### 2.2.2. Perturbations

Initially, at  $t = 0$  s, we perturb the model equilibrium by launching, at the bottom boundary, simultaneously time-dependent signals in the ion and neutral gas pressures, which are expressed as follows:

$$\begin{aligned} p_{[i,n]}(x, y, t = 0) &= p_0 \left( 1 + A_{p[i,n]} \exp\left(-\frac{x^2 + (y - y_0)^2}{w^2}\right) f(t) \right), \\ f(t) &= \begin{cases} 1 - \exp(-t/\tau), & t \leq \tau_{\max} \\ \exp(-(t - \tau_{\max})/\tau), & t > \tau_{\max} \end{cases}. \end{aligned} \quad (14)$$

Here  $y_0$  is the vertical position of the signals,  $w$  is their width and  $A_{p_i}$ ,  $A_{p_n}$  their amplitudes. Function  $f(t)$  denotes the

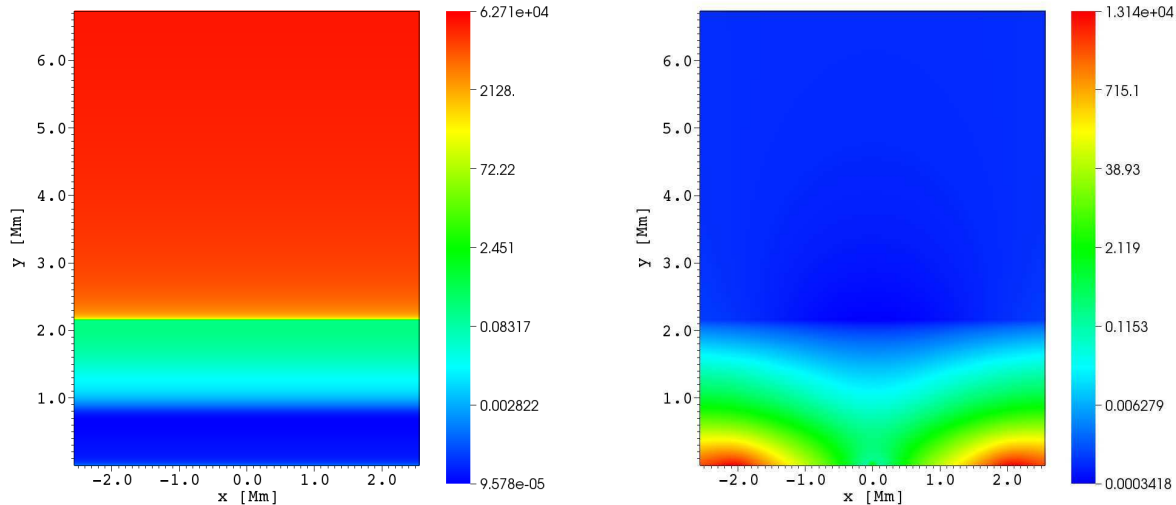


**Figure 3.** Ratio of the mass density of ions to the mass density of neutrals (left) and plasma beta (right) at the plasma equilibrium.

temporal profile of the gas pressure signal, with  $\tau$  being its characteristic growth/decay time and  $\tau_{\max}$  time at which  $f(t)$  reaches its maximum. We set and hold fixed  $w = 0.1$  Mm,  $\tau = 50$  s and  $\tau_{\max} = 30$  s, while allowing other parameters to vary. For our studies, the signal position,  $y_0$ , varies between 1.65 Mm and 1.85 Mm and the amplitude  $A_p$  between 6 and 10. This signal position corresponds to a region of  $\beta < 1$  (Figure 3, right). As a result of that, slow and fast magnetoacoustic waves are weakly coupled there and the initial pulse triggers slow waves, which propagate essentially along magnetic field lines (e.g. Nakariakov & Verwichte 2005). Unless otherwise stated, the further analysis focuses on the case for  $A_p = 8$  and  $y_0 = 1.75$  Mm, which corresponds to plasma heated to maximum temperature of 60 kK 1.75 Mm above the photosphere. We have verified that only such strong pulses launched at the top of the chromosphere result in spicules. Lower amplitude pulses excite smaller jets and pulses launched from the lower chromospheric layers lead to horizontally spread jets. The time-dependent signal launched at  $y_0 = 1.75$  Mm may mimic a post-reconnection event.

### 3. NUMERICAL SIMULATIONS OF TWO-FLUID EQUATIONS

To solve two-fluid equations numerically, we use the JOANNA code (Wójcik et al. 2017, in preparation). In our problem, we set the Courant–Friedrichs–Lewy number (Courant et al. 1928) equal to 0.3 and specify the simulation box in  $(x, y)$  as  $(-1.28, 1.28)$  Mm  $\times$   $(1.75, 50.0)$  Mm, where  $y = 0$  denotes the bottom of the photosphere. In the numerical simulations we adopt the uniform grid within the region  $(-1.28 \leq x \leq 1.28)$  Mm  $\times$   $(1.75 \leq y \leq 6.87)$  Mm, which is covered by  $256 \times 512$  grid points. This grid leads to a resolution of 10 km in the main region of the simulation box that

is below  $y = 6.12$  Mm. Above this region, namely within the rectangle  $(-1.28 \leq x \leq 1.28)$  Mm  $\times$   $(6.87 \leq y \leq 50.0)$  Mm, we implement a stretched grid along the  $y$ -direction; this box is divided into 128 cells whose size grows with  $y$ . Such a stretched grid plays the role of a sponge as it absorbs incoming signal and minimizes reflections from the top boundary. We impose open boundary conditions for out-flowing signal at the side boundaries, while at the top and bottom we fixed all plasma quantities to their equilibrium values.

We launch the gas pressure signals in the chromosphere varying their initial position,  $y_0$ , and amplitudes,  $A_{p_i}$  and  $A_{p_n}$ , as described in Section 2.2.2. The basic mechanism behind the simulations is that the signals, while launched from the region of  $\beta < 1$ , essentially split into two, counter-propagating along the equilibrium magnetic field lines' slow magnetoacoustic (slow henceforth) waves; downwardly propagating slow waves decay in time (not shown in the framework of these simulations), while upwardly moving slow waves grow in their amplitudes. The latter convert into a slow shock at higher altitudes due to the decrease of mass density with height. The chromospheric plasma lags behind the shock front to form a contact wave consisting of a spicule. The simple waves structure associated with this phenomenon is described by Kuźma et al. (2017). Note that the signal in  $A_{p_i}$  excites fast magnetoacoustic waves too but they are of low amplitudes as they spread quasi-isotropically in space. The pulse in  $A_{p_n}$  generates neutral acoustic waves (Zaqarashvili et al. 2011).

The top row of Figure 4 shows the spatial profiles of  $\log(\varrho_i(x, y))$  at three instants of time, which are  $t = 70$  s (top left),  $t = 210$  s (top middle) and  $t = 320$  s (top-right).

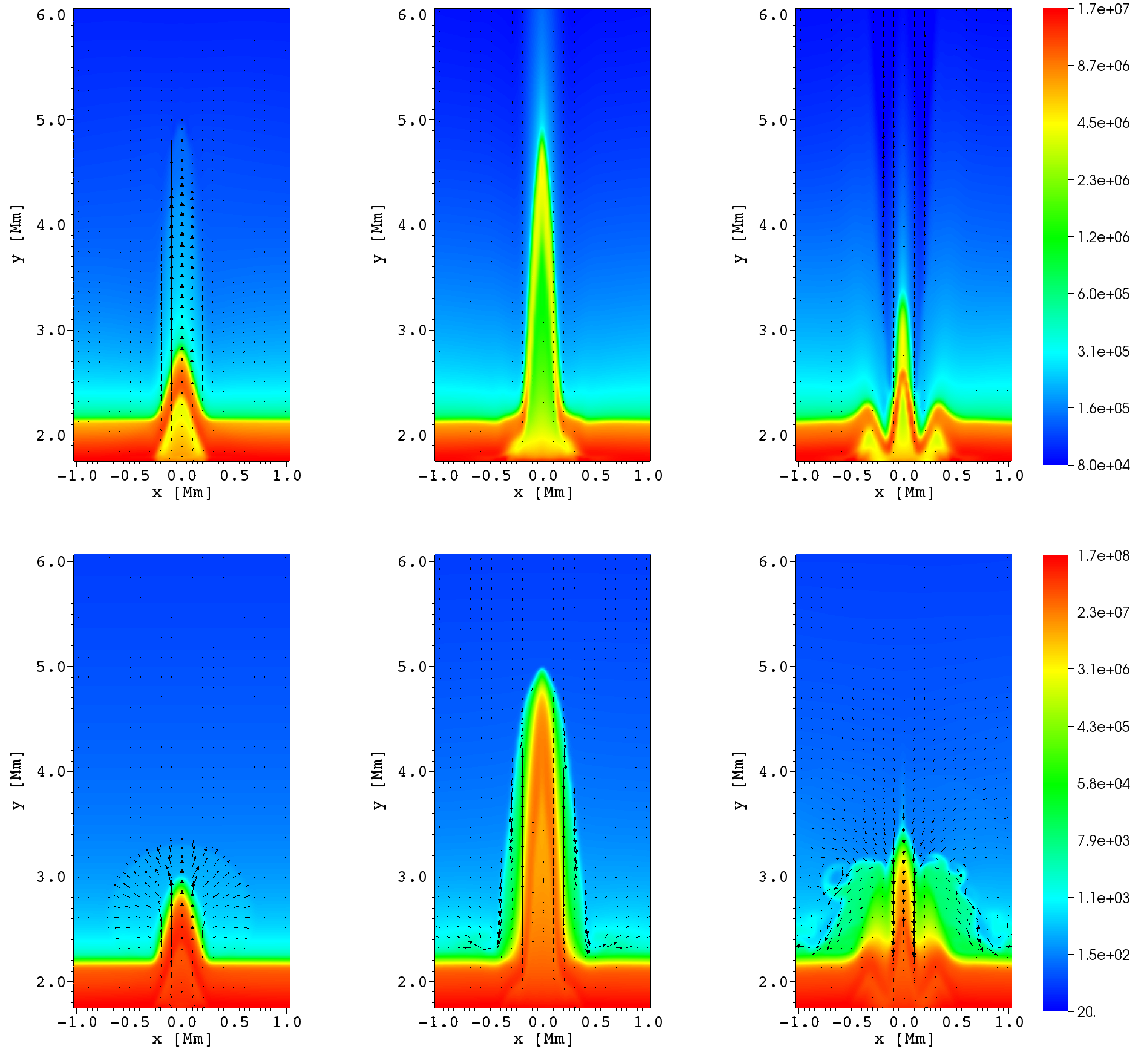


**Figure 4.** Temporal evolution of  $\log(Q_i(x, y))$  at  $t = 70$  s,  $t = 210$  s, and  $t = 320$  s (from top left to top right), and  $\log(Q_n(x, y))$  (from bottom left to bottom right). Arrows represent ion and neutral velocity vectors in the  $x - y$  plane. Hot coronal plasma is blue, cold chromospheric plasma is orange-red, and intermediate transition region plasma/interface between them is green on the colormap.

The gas pressure drivers of Eq. (14) operate at the point of  $(x = 0, y = y_0 = 1.75)$  Mm, which is located in the chromosphere around 0.35 Mm below the TR, and they reach their maximum at  $t = 30$  s. At  $t = 70$  s, it is found that the ion shock front is followed by hot plasma, which results from the drivers, and it reaches a level of  $y \approx 5.0$  Mm. It is followed by a second, stronger shock, which results at maximum of  $f(t)$ . However, the chromospheric (cold) ion plasma is located at  $y \approx 2.8$  Mm at this time (see Figure 4, the top-left panel). The shock fronts move continuously upward, which attain the level of more than  $y = 25$  Mm (not drawn here) and the chromospheric plasma reaches its maximum height of  $y \approx 4.9$  Mm at  $t = 210$  s (Figure 4, the top-middle panel). The head of the spicule remains denser (yellow color on the colormap), while its interior rarefies in time (green color on the colormap) due to rarefaction wave propagating upwards.

Above the apex of the ion spicule, we can see a constant stream of ions injected into higher layers of the solar corona. In addition, the down-falling of the ion spicule plasma also starts as the time progresses. The reverse velocity arrows in the central region and sides of the ion spicule justifies down-fall of the cold chromospheric plasma. This downfall is more stronger during the decay phase (see reverse velocity arrows in the top-middle and top-right panels), which creates the V-shaped structure as the down-falling velocity is non-uniform along the horizontal direction (see the top-right panel).

We have implemented two-fluid approach in our numerical experiment to understand the behavior of ions and neutrals in the spicule dynamics. It may be possible that the ions and neutrals may exhibit the different dynamics. Therefore, we show the corresponding profiles of  $\log(Q_n(x, y))$  in the bottom panels of Figure 4. The overall dynamics of the neu-

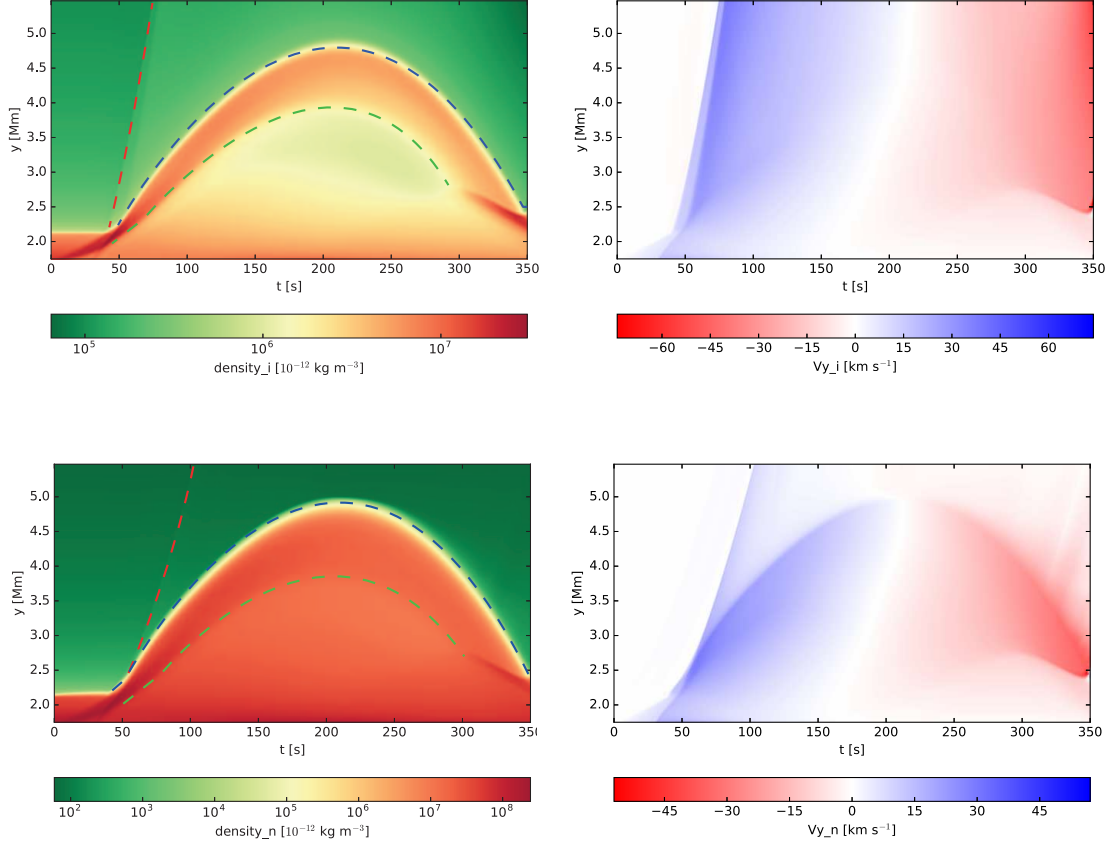


**Figure 5.** Temporal evolution of  $\log(Q_{i,n}(x = 0, y))$  (left) and  $V_{i,n,y}(x = 0, y)$  (right) for the ions (top) and neutrals (bottom). The red, blue, and green dashed lines indicate slow shock, contact wave, and rarefaction wave, respectively. Transition from the red to the green area shows the contact waves.

trals (i.e., formation of a shock front and lagging off chromospheric plasma) are qualitatively similar to the dynamics of ions in this numerical experiment. However, the slow neutral shock does not propagate along magnetic field lines, forming a circle-like front (the left bottom panel). There is also no upward stream consisting of neutrals above the apex of the ion spicule (the bottom-middle panel). The spicule is surrounded by the neutral cloud in which we can spot vortices of Rayleigh-Taylor instabilities during decay phase. The down-falling of neutral gas is very weak during maximum phase (the middle right-panel), which is mostly dominated towards the edges of the neutral spicule. However, strong down-flow of neutral gas occurs during the decay phase. Neutral spicule has V-shaped structure resemblance in the decay phase (bottom-right panel) but not as prominent as it occurs in the ion spicule. As neutrals are not guided by the magnetic field, the neutral gas experiences more horizontal spread compared to the ions. So, the neutral spicule does not exhibit very sharp V-shaped structure due to the dominance of horizontal spreading of neutrals.

In addition, the top of the ion (neutral) spicule is suppressed till the height of  $y = 3.4$  Mm ( $y = 3.5$  Mm) due to the dominance of down-falling in the decay phase. This down-falling is strongest on sides of the ion/neutral spicule and decrease outwards, which creates the V-shape structure at the bottom of ion/neutral spicules. Most of the chromospheric plasma, which was injected into the corona falls toward the chromosphere/TR.

We estimate now the width of the spicule in neutrals and ions at  $y = 3.0$  Mm during the maximum phase of the spicule. By looking at horizontal mass density profiles and assuming that the mass density above (below) 1.2 times of the background mass density (i.e., mass density in the absence of any spicule; at  $x = -1.0$  Mm) are considered as the starting (end) points of the spicules. We find that the neutral spicule is wider ( $\sim 600$  km) than the spicule consisting of ions ( $\sim 400$  km).

We discuss now temporal evolution of mass densities and vertical velocities of ions and neutrals. Figure 5 displays time signatures of  $Q_{i,n}(x = 0, y, t)$  (the left panels) and  $V_{i,n,y}(x = 0, y, t)$  (the right panels) for ions (the top panels)

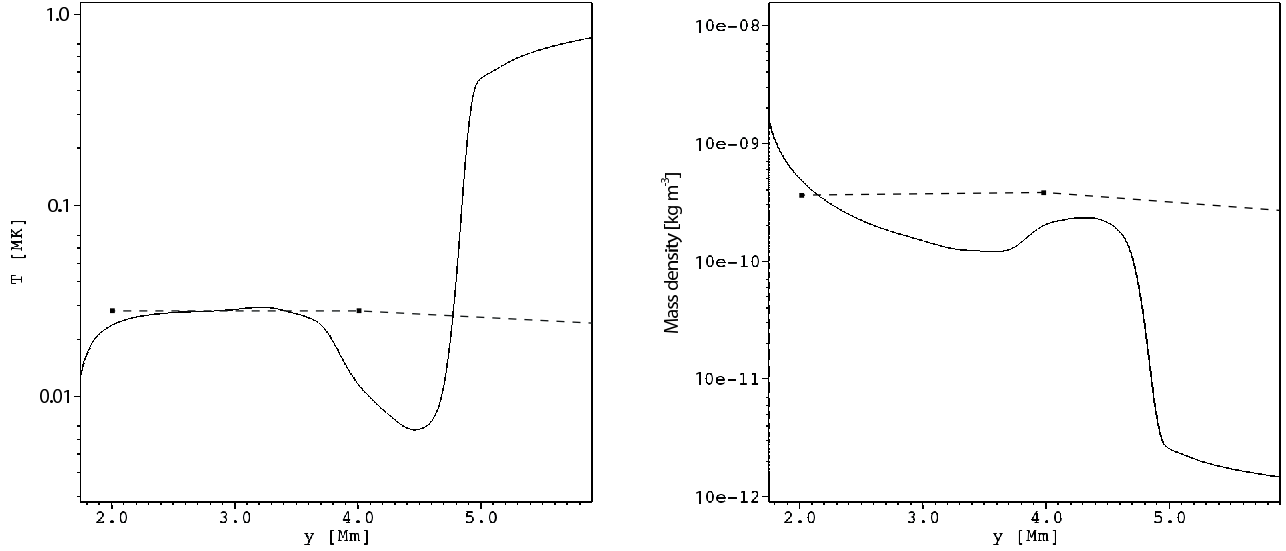


**Figure 6.** Vertical profiles of average temperature (the left panel) and mass density (the right panel) of the spicule in the simulation evaluated along  $x = 0$  Mm, at  $t = 210$  s (the solid lines) and observational data of [Beckers \(1968\)](#) (the dashed lines).

and neutrals (the bottom panels). The rise time of the chromospheric ions to their maximum height is about 210 s (see Figure 5, top-left). In the temporal evolution profile of the ions, we spot three major waves above the TR (the top-left panel): the leading wave is a slow shock wave (red line) that is followed by the contact wave (blue line) and the rarefaction wave (green line). The contact wave does not appear in the top-right panel since there is no jump in velocity of ions across a contact surface with normal almost perpendicular to **B**. See also [Kuźma et al. \(2017\)](#) for a similar discussion in the MHD case. The light-green area between slow shock and contact wave reveals that significant amount of ions are constantly injected above the spicule apex during its lifetime. This phenomenon is absent in the case of neutrals (the bottom-left panel). The ion slow shock travels with higher speed ( $\sim 150$  km  $s^{-1}$ ) than neutral slow shock ( $\sim 90$  km  $s^{-1}$ ; see the right panels). Both ions and neutrals injected into the corona above the spicule apex accelerate with height. The light-green area below the apex of the ion spicule reveals that the rarefaction wave exerts a greater impact on the already rarefied ion spicule. The boundary between chromospheric and coronal neutrals is also sharper than between chromospheric and coronal ions. This is a result of merging between the top of the ion spicule and highly ionized corona. From the temporal evolution profile of the neutrals, we infer that both shock and rarefaction waves are of low amplitudes, to the point, when the rarefaction wave is almost unnoticeable (green line, the bottom-left panel). At a later time, the chromospheric plasma, which was earlier injected into the corona, begins to fall toward the TR.

The spicule consists mostly of dense and cold neutrals. The ionization level at all stages of the spicule evolution remains at about 10%. Figure 6 (left) shows the vertical profile of the average temperature of the simulated spicule (solid line) along with the widely used observed values (dashed line; [Beckers 1968](#)). The average temperature of the spicule (solid line) is 100 times lower than the coronal plasma, which shows a constant value of temperature up to a height of  $\sim 2.8$  Mm. The spicule plasma exhibits its lowest temperature of 9000 K in the upper part of the spicule,  $\sim 4500$  km above the TR. Higher up, the temperature experiences an abrupt jump at the contact wave, reaching temperatures of up to 800,000 K and matching the local coronal temperature. Figure 6 (left) shows the vertical profile of mass density of the spicule (solid line). The cold head of the spicule is about twice denser than its core, which is resembled by the weak bump around  $y = 4.2$  Mm. Above the apex of the spicule, mass density decreases to its coronal values. The temperature as well as mass density of the simulated spicule are compared with the classical results of the spicule (dashed line in both-panels of Figure 6; [Beckers 1968](#)). Observationally, it is reported that mass density and temperature are almost constant over the whole length of the spicule, which vary by about 10 % over the whole length of the spicule ([Beckers 1968](#)). However, the simulated spicule exhibits a significant variations in the temperature and mass density along its length. It should be noted that the temperature of the spicule matches with the observed values over a height range of  $2.0$  Mm  $< y < 3.7$  Mm.

We now discuss gradients of gas pressures of neutrals and ions. The corresponding vertical profiles are displayed in Figure 7. The dotted line shows the gas pressure gradient

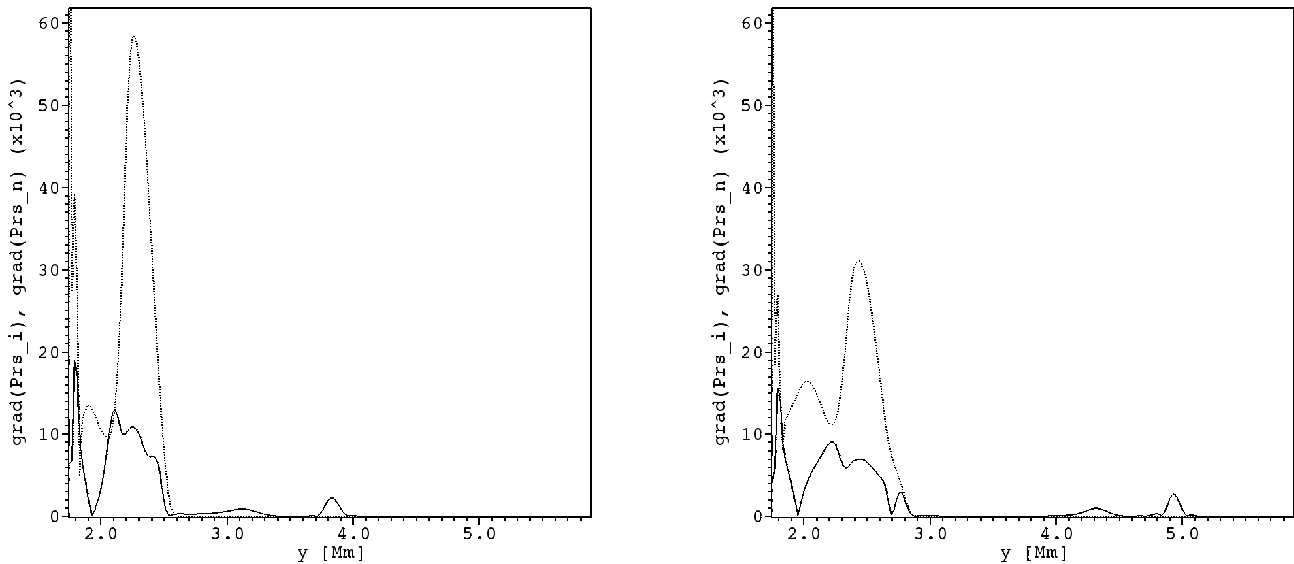


**Figure 7.** Vertical profiles of the gas pressure gradient of neutrals (the dotted line) and ions (the solid line) evaluated along  $x = 0$  Mm, at  $t = 60$  s (the left panel) and  $t = 70$  s (the right panel).

of neutrals, while the solid line illustrates the gas pressure gradient of ions along the  $y$ -direction. The left (right) panel illustrates the vertical distribution of the gas pressure gradient at  $t = 60$  s ( $t = 70$  s). It is clear that the neutral gas pressure gradient (the dotted line) is very high in comparison to the ion gas pressure gradient (the solid line) at these instants of time. The difference between neutrals and ions pressure gradients is higher at about  $y = 1.75$  Mm at which the driver in gas pressures operates. The gradients approach each other far away from the driver. The significant gas pressure gradient difference between the ions and neutrals is an important result, which clearly leads to a different dynamics of ions and neutrals.

#### 4. DISCUSSIONS AND CONCLUSIONS

We have performed numerical simulations of a spicule by setting in the upper chromosphere localized time-dependent signals in ion and neutral gas pressures. The initial magnetic field configuration was current-free, and the atmosphere was stratified hydrostatically. The whole physical system was described by a set of two-fluid equations. Our numerical findings revealed that, as a result of the rapid decrease of the mass density with height, an upwardly propagating signal quickly steepens into a shock. This shock propagates along the magnetic field lines, reaching the low solar corona, and is followed by the chromospheric plasma, which consists of the cold and dense jet (spicule). This jet exhibits properties of a contact wave (Kuźma et al. 2017) and reaches up to a certain height (typically 4-6 Mm) and then returns to the chromosphere. The mean upflow speed was 20-25 km  $s^{-1}$ . The comparison between the numerical and observa-

tional data always enlightens the path to go further. Therefore, we tried to compare the observed properties of the simulated spicule with the various spicule observations. Beckers (1968, 1972) reported that the average height of spicules can vary from 6500 km to 9500 km. Similarly, Lippincott (1957) reported the spicule height range from 7000 km to 13,000 km and Pasachoff et al. (2009) inferred these numbers from 4200 km to 12,200 km. Observed upward velocity of spicules exhibits variations within the range of 20.0-150.0 km  $s^{-1}$  (De Pontieu et al. 2007b) and 3.0-75.0 km  $s^{-1}$  (Pasachoff et al. 2009). The numerically obtained value of spicule height ( $\sim 4.9$  Mm) and upward velocity ( $\sim 20$ -25 km  $s^{-1}$ ) of the simulated spicule lies in the observed range of height and velocity (Beckers 1968, 1972; De Pontieu et al. 2007b; Pasachoff et al. 2009). It should also be noted that the numerical values of the spicule match with those obtained for MHD (Kuźma et al. 2017).

Novelty of our numerical simulations lies in the usage of the two-fluid model, which was not investigated so far. The two-fluid simulations invoke real physical conditions of the lower solar atmosphere and plasma processes within various localized jets. It is noteworthy that a significant role of neutrals associated with confined pseudo-shocks in carrying substantial energy and mass into the overlying solar atmosphere was discovered by Srivastava et al. (2017). The key findings of our simulations can be summarized as follows. (a) The spicule dynamics is slightly different in ions and neutrals; (b) the core of the spicule is dominated by cold neutrals; (c) the neutral spicule is wider compared to the ion spicule; (d) the ionization remains essentially still with height and horizontal distance within the spicule, only the top of the spicule

is significantly ionized; and (e) in later moments of time of the spicule evolution higher amplitude of the slow rarefaction wave for the ion spicule results in a different structure than for the neutral spicule. The general scenario of the rise and the downfall of the spicule is the same for ions and neutrals and it is close to that for MHD (Kuźma et al. 2017). The dispatches in gas pressure gradients between ions and neutrals is a key factor to understand the minor differences in the dynamics of ions and neutral spicules. Obviously, the magnetic field does not have any direct influence on the dynamics of neutrals, while the motion of ions is affected by the magnetic field directly. The direct influence of the magnetic field on the ions controls the width of the ion spicule. Therefore, the ion spicule is a very well collimated column of ions with its small width. In the absence of the influence of magnetic field, the neutrals get extra freedom to propagate in the horizontal direction; a constraint on them results from ion-neutral collisions. As a result, the neutral spicule is wider compared to the ion spicule. The V-shaped structure near the base of the ion/neutral spicule is an interesting phenomenon of these simulations, which results from down-falling gas. As ions are affected by magnetic field, the well collimated down-falling ion gas results in, which exerts the gas pressure force producing in the decay phase the sharp V-shaped structure near the base of the ion spicule.

Most of observations reveal that temperature and mass density of a spicule remain essentially constant along its height (Beckers 1968, 1972; see also review article by Sterling 2000). However, our simulated spicule shows a significant variations in its temperature as well as mass density. The temperature of the spicule is constant upto the height of  $y = 3.5$  Mm, while higher up the temperature falls off abruptly. The constant phase of temperature matches the observational findings. However, there is a sharp increase in the temperature above  $y = 4.5$  Mm, which may suggest that the thermal evolution of the cold chromospheric plasma can

be important as proposed by Pereira et al. (2014). Overall, the mass density of the spicule is decreasing with height, which is qualitatively consistent with the observed mass densities (Beckers 1968). However, the top of the spicule shows slightly higher densities. The high temperature near the top-part of the spicule significantly ionizes the neutrals, which were taken into account in the present scenario. Recently, Pereira et al. (2014) reported that spicules undergo thermal evolution using high-resolution observations. Spicules produce more emission near their bases compared to their apexes at chromospheric temperature (i.e., Ca II H & K and Mg II h & k lines). However, bases of spicules become dark and the top parts of spicules lead to more emissions at the TR temperature (i.e., Si IV;  $T = 80$  kK). This observational finding predicts that ionization grows with height within the spicule, which is successfully reproduced by our two-fluid numerical simulations of spicules.

In conclusion, our numerical simulations of the spicule performed within the framework of the two-fluid approach successfully mimics the averaged properties of classical spicules. Ion and neutral spicules follow the similar dynamics in terms of rise time and peak altitude. The core of the spicule exhibits an abundance of neutrals, with growing in time rarefaction of ions.

The authors express their thanks to the referee for his/her comments on the earlier version of the draft. This work was financially supported by the project from the National Science Centre, Poland, (NCN) Grant No. 2014/15/B/ST9/00106. The JOANNA code used in this work was developed by Mr. Darek Wójcik. These numerical simulations were performed on the LUNAR cluster at Institute of Mathematics of University of M. Curie-Skłodowska. Visualization of the simulations data was done with the use of IDL (Interactive Data Language) and VisIt software packages.

## REFERENCES

- Avrett, E. H., & Loeser, R. 2008, *ApJS*, 175, 228
- Beck, C., Rezaei, R., Puschmann, K. G., & Fabbian, D. 2016, *SoPh*, 291, 2281
- Beckers, J. M. 1968, *SoPh*, 3, 367
- . 1972, *ARA&A*, 10, 73
- Cheng, Q.-Q. 1992, *A&A*, 266, 537
- Courant, R., Friedrichs, K., & Lewy, H. 1928, *Mathematische Annalen*, 100, 32
- Cranmer, S. R., & Woolsey, L. N. 2015, *ApJ*, 812, 71
- . 2016, *ApJ*, 822, 119
- De Pontieu, B., Erdélyi, R., & James, S. P. 2004, *Nature*, 430, 536
- De Pontieu, B., Hansteen, V. H., Rouppe van der Voort, L., van Noort, M., & Carlsson, M. 2007a, *ApJ*, astro-ph/0701786
- De Pontieu, B., McIntosh, S. W., Hansteen, V. H., & Schrijver, C. J. 2009, *ApJL*, 701, L1
- De Pontieu, B., McIntosh, S., Hansteen, V. H., et al. 2007b, *PASJ*, 59, S655
- Haerendel, G. 1992, *Nature*, 360, 241
- Hansteen, V. H., De Pontieu, B., Rouppe van der Voort, L., van Noort, M., & Carlsson, M. 2006, *ApJL*, 647, L73
- Hegglund, L., De Pontieu, B., & Hansteen, V. H. 2007, *ApJ*, 666, 1277
- Hirayama, T. 1992, *SoPh*, 137, 33
- Hollweg, J. V. 1972, *Cosmic Electrodynamics*, 2, 423
- . 1982, *ApJ*, 257, 345
- Hollweg, J. V., Jackson, S., & Galloway, D. 1982, *SoPh*, 75, 35

- James, S. P., Erdélyi, R., & De Pontieu, B. 2003, *A&A*, 406, 715
- Konkol, P., Murawski, K., & Zaqarashvili, T. V. 2012, *A&A*, 537, A96
- Kopp, R. A., & Kuperus, M. 1968, *SoPh*, 4, 212
- Kudoh, T., & Shibata, K. 1999, *ApJ*, 514, 493
- Kuźma, B., Murawski, K., Zaqarashvili, T. V., Konkol, P., & Mignone, A. 2017, *A&A*, 597, 133
- Lippincott, S. L. 1957, *Smithsonian Contributions to Astrophysics*, 2, 15
- Madjarska, M. S., Vanninathan, K., & Doyle, J. G. 2011, *A&A*, 532, L1
- Matsuno, K., & Hirayama, T. 1988, *SoPh*, 117, 21
- McIntosh, S. W., & De Pontieu, B. 2009, *ApJ*, 707, 524
- McIntosh, S. W., Innes, D. E., De Pontieu, B., & Leamon, R. J. 2010, *A&A*, 510, L2
- Moore, R. L., & Fung, P. C. W. 1972, *SoPh*, 23, 78
- Murawski, K., & Zaqarashvili, T. V. 2010, *A&A*, 519, A8
- Nakariakov, V. M., & Verwichte, E. 2005, *LRSP*, 2, 3
- Nishikawa, T. 1988, *PASJ*, 40, 613
- Pasachoff, J. M., Jacobson, W. A., & Sterling, A. C. 2009, *SoPh*, 260, 59
- Pereira, T. M. D., De Pontieu, B., & Carlsson, M. 2012, *ApJ*, 759, 18
- Pereira, T. M. D., Rouppe van der Voort, L., & Carlsson, M. 2016, *ApJ*, 824, 65
- Pereira, T. M. D., De Pontieu, B., Carlsson, M., et al. 2014, *ApJL*, 792, L15
- Roberts, B. 1979, *SoPh*, 61, 23
- Roberts, W. O. 1945, *ApJ*, 101, 136
- Rouppe van der Voort, L., De Pontieu, B., Pereira, T. M. D., Carlsson, M., & Hansteen, V. 2015, *ApJL*, 799, L3
- Secchi, P. A. 1887, *Le Soleil*, vol. 2 (Gauthier-villas, Paris)
- Skogsrud, H., Rouppe van der Voort, L., & De Pontieu, B. 2014, *ApJL*, 795, L23
- Skogsrud, H., Rouppe van der Voort, L., De Pontieu, B., & Pereira, T. M. D. 2015, *ApJ*, 806, 170
- Smith, P. D., & Sakai, J. I. 2008, *A&A*, 486, 569
- Srivastava, A. K., Murawski, K., Kuźma, B., et al. 2017, *NatAs*, under review
- Sterling, A. C. 2000, *SoPh*, 196, 79
- Sterling, A. C., & Hollweg, J. V. 1984, *ApJ*, 285, 843
- Sterling, A. C., & Mariska, J. T. 1990, *ApJ*, 349, 647
- Sterling, A. C., & Moore, R. L. 2016, *ApJL*, 828, L9
- Sterling, A. C., Moore, R. L., & DeForest, C. E. 2010, *ApJL*, 714, L1
- Sterling, A. C., Shibata, K., & Mariska, J. T. 1993, *ApJ*, 407, 778
- Suematsu, Y. 1998, in *Solar Jets and Coronal Plumes*, ESA Special Publication, Vol. 421, ed. T.-D. Guyenne, 19
- Suematsu, Y., Ichimoto, K., Katsukawa, Y., et al. 2008, in *Astronomical Society of the Pacific Conference Series*, Vol. 397, *First Results From Hinode*, ed. S. A. Matthews, J. M. Davis, & L. K. Harra, 27
- Suematsu, Y., Shibata, K., Nishikawa, T., & Kitai, R. 1982, *SoPh*, 75, 99
- Suematsu, Y., Wang, H., & Zirin, H. 1995, *ApJ*, 450, 411
- Tian, H., McIntosh, S. W., Habbal, S. R., & He, J. 2011, *ApJ*, 736, 130
- Tsiropoula, G., Tziotziou, K., Kontogiannis, I., et al. 2012, *SSRv*, 169, 181
- Wójcik, D., Murawski, K., & Zaqarashvili, T. V. 2017, *A&A*, in preparation
- Zaqarashvili, T. V., & Erdélyi, R. 2009, *SSRv*, 149, 355
- Zaqarashvili, T. V., Khodachenko, M. L., & Rucker, H. O. 2011, *A&A*, 529, A82